3D-printing of ceramic filaments with ductile metallic cores

Qiaosong Cai [a], Sylvain Meille [b], Jérôme Chevalier [b], Shitong Zhou [a], Florian Bouville [a], Iuliia Tirichenko [a], Eduardo Saiz [a,*]
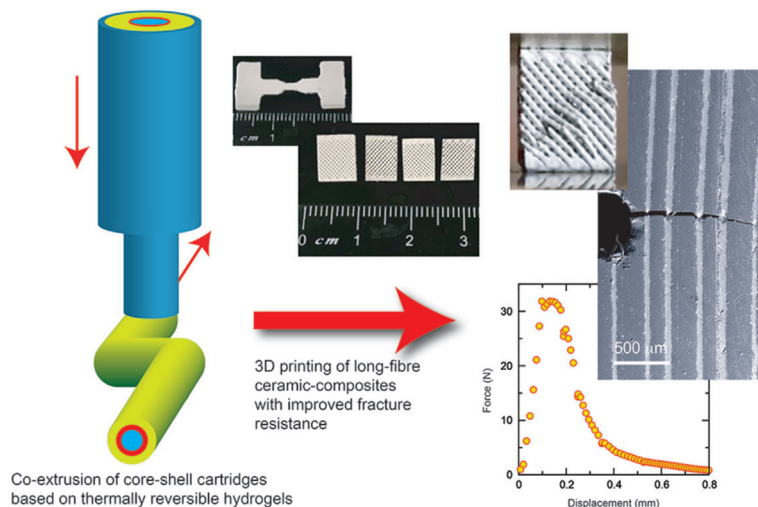
[a] Centre for Advanced Structural Ceramics, Department of Materials, Imperial College of London, United Kingdom
[b] Univ Lyon, INSA Lyon, UCBL, CNRS, MATEIS, UMR5510, 69621 Villeurbanne , France

HIGHLIGHTS

- Development of a co-extrusion approach for the additive manufacturing of ceramics reinforced by thin (25–100 μm), continuous steel fibres.
- The technique allows the introduction of thin (10–50 μm) interphases between the fibre and the matrix.
- The materials exhibit works of fracture up to 1400 J/m^2, two orders of magnitude above the ceramic matrix.

GRAPHICAL ABSTRACT

Co-extrusion of core-shell cartridges based on thermally reversible hydrogels

3D printing of long-fibre ceramic-composites with improved fracture resistance

ARTICLE INFO

ABSTRACT

The additive manufacturing of composite structures can open possibilities in the design and fabrication of devices but also demands new approaches. In this work, we use thermally reversible pastes to fabricate ceramic matrix (Al_2O_3) composites reinforced with continuous metallic fibres (steel). The approach is based on the micro-extrusion of ceramic–metal filaments with core–shell and layered arrangements. These filaments are employed in the additive manufacturing of dense and light-weight cellular structures that combine the stiffness and strength of the ceramic shell with the fracture resistance and energy absorption capabilities provided by the metal core. The approach can be used to extrude filaments with thin porous interlayers separating the core and the shells to create a weak fibre/matrix interphase. The cellular structures fabricated with these filaments exhibit higher compressive strengths and energy absorption capabilities than those fabricated from pure ceramics. The works of fracture of the dense composites are one to two orders of magnitude above those of the ceramic matrix (10^3 J/m^2) while the bending strengths remain comparable to those of 3D printed alumina (200–350 MPa). The technique could be easily extended to other material combinations opening new opportunities in the additive manufacturing of multi-material parts and devices.

* Corresponding author.
  E-mail address: e.saiz@imperial.ac.uk (E. Saiz).

1. Introduction

Progress in a wide range of technologies, from transportation to healthcare, demands light-weight structures able to operate in demanding environments and under complex loading requirements. In many of these cases ceramic-based materials are the only viable alternative. Most ceramics have low density and are relatively inert in oxidizing or corrosive atmospheres. However, brittleness hampers their practical use. A way around this major limitation is to develop ceramic composites with structures designed to improve toughness. Multiple approaches have been developed, from transformation toughening to intricate fiber arrangements in ceramic matrices. These materials are successfully used in a wide range of fields, from healthcare to aerospace but, in general, their practical implementation is still modest [1–3]. In part, this is due to the inherent complexity associated to the development of effective strategies to significantly increase fracture resistance in ceramics while retaining strength and stiffness. In addition, the design and fabrication of complex-shaped parts retaining the desired mechanical performance can also be problematic. These challenges are driving a significant research effort that spans different fields from manufacturing to modelling or advanced characterization. Here, like in many other cases, success will depend on our ability to combine careful microstructural control with the fabrication of large components with complex shapes.

Additive manufacturing has emerged as a promising alternative for the manufacturing of ceramic parts with complex shapes. It could also create new opportunities for the microstructural manipulation of composites [4,5]. For instance, extrusion-based printing has been used to build brick and mortar composites inspired by natural designs or to manipulate the alignment of short-fibers in polymeric and ceramic matrices [6–9]. However, multimaterial printing is proving difficult. In addition, high-performing, fiber-reinforced composites are based on long or continuous fibers and require careful engineering of fiber–matrix interphases [1,10]. If these features could be incorporated in additive manufacturing, they could open new opportunities in the design of high-performance composite structures and devices. At the macroscopic scale, they could allow the fabrication of complex parts that are now unreachable with standard processes. At the microscale they will enable the rational implementation of microstructures specifically designed to optimize the mechanical or functional response.

In this work we show how Direct Ink Writing (DIW) can be used to print ceramic-composite structures combining high strength, toughness and stiffness by using filaments with a core shell structure. Co-extrusion has been used before to fabricate dense ceramics with fibrous, layered or brick and mortar architectures. These are often thermoplastic-based systems that cannot be easily adapted to do 3D printing because they rely on multiple consecutive extrusion steps to refine the microstructural dimensions [11–14]. When it comes to printing, most of the work has been done with polymer-based composites. Polymer lattices combining high stiffness and toughness have been printed using core–shell filaments with co-extrusion systems that required specially designed printing heads with concentric cylinders [15,16]. Co-extrusion has also been used to build optical waveguides [17], biopolymers [18], polymer composites [19], fiber based supercapacitors with organic binders [20] or shape memory polymers containing metallic fibers [21,22]. In the latter case, the long metallic fibers are co-extruded as a wire inside the polymer shell. However, in the case of ceramics, the few examples of printing core–shell filaments using similar set-ups, mostly deal with the extrusion of filaments with sacrificial or hollow cores [8,23]. The concentric printing head increases the complexity of the set-up and bounds the filament diameters.

Here, we describe an approach, based on the use of thermally reversible hydrogels to create cartridges with a core–shell structure that can be extruded through a single nozzle at room temperature, simplifying the system and reducing the core diameter. Xia et al. [9] used a frozen rod to form a core in a printing cartridge that could also be extruded through a single nozzle. Their approach results in cores significantly larger in diameter containing short fibers that align during extrusion. In the present work, the fibers form "in situ" during printing and firing. Although this adds the constraint of a compatible sintering temperature for core and shell, it enables the printing of ceramics reinforced with long, continuous fibers, something that, so far, has been difficult to achieve. The cartridges can contain one or multiple cores and can be used to print dense parts with complex shapes and cellular structures reinforced by continuous fibers with diameters that can go below 50 μm. The approach also enables the extrusion of filaments with thin interlayers between the core and the shell that can be used to engineer a fiber matrix interphase. We demonstrate this concept by extruding filaments with a hard and brittle shell (Al_2O_3) and a ductile core (steel, 430L) and show how this approach allows the fabrication of cellular and dense structures that retain the ceramic strength and stiffness but exhibit enhanced fracture resistance.

2. Experimental

Pluronic F-127® solutions with concentrations ranging from 15 wt% to 40 wt% were prepared by stirring flasks of deionised water mixed with the proper amount of Pluronic powders (Sigma Aldrich) at 4 ℃. The solutions were left in a fridge at 4 ℃ for 24 h to dissolve the powders and release the bubbles until they become clear and homogeneous. To prepare the printing pastes, the suspensions were cooled to ∼ 0 ℃ in an ice bath in a 150 ml poly tetra fluoroethylene container and the different powders (alumina and steel) were added with 0.5 wt% (with respect to the powder content) Dolapix CA (Zschimmer & Schwarz, Germany) to promote dispersion. The alumina powders (Baikalox B-Series, SMA6, 99.99 %, D_{50} = 0.2 μm, Baikowski, France) were sieved through a 100 μm mesh to break large aggregates. Stainless steel (430L Cr: 16–18) powders with average particle size of ∼ 5 μm were purchased from US Research Nanomaterials and fine synthetic graphite powders (APS 7–11 μm, 99 %) from Alfa Aesar.

Pastes for direct ink writing were prepared by mixing Pluronic solutions and inorganic powders using a planetary centrifugal mixer (Thinky ARE-250, USA) at 2000 rpm for 2 min. The process was repeated several times (4 to 6 times depending on the solid loading and the total volume of paste). The pastes were then defoamed at room temperature at 2200 rpm for 5 min to remove bubbles. They could be stored at room temperature for a period up to 2 months without water segregation, drying or cracking.

Filaments with core shell structures were extruded using a single cylindrical or conical nozzle with diameters varying between 100 and 1500 μm. To do this we took advantage of the temperature-dependent response of pastes based on the thermally reversible behavior of Pluronic 127^R hydrogels. Cartridges with different core–shell structures were prepared by using a set of spacers to create cylindrical holes in the gel pastes that can then be filled with a flowing suspension that is subsequently gelled (Fig. 1). First a 10 ml syringe (15.6 mm diameter) was immersed in an ice bath and filled with a flowing alumina suspension at 0℃. Subsequently, the syringe is placed in a hot bath (70℃) to gel and one large cylindrical spacer or multiple small ones are inserted. The diameters of the spacers were 4.5 or 8 mm. The spacers were removed leaving one or several cylindrical holes that are then filled with a flowing steel paste kept at 0℃. At this low temperature the viscosity of the pastes is low and they flow to fill the syringes without trapping
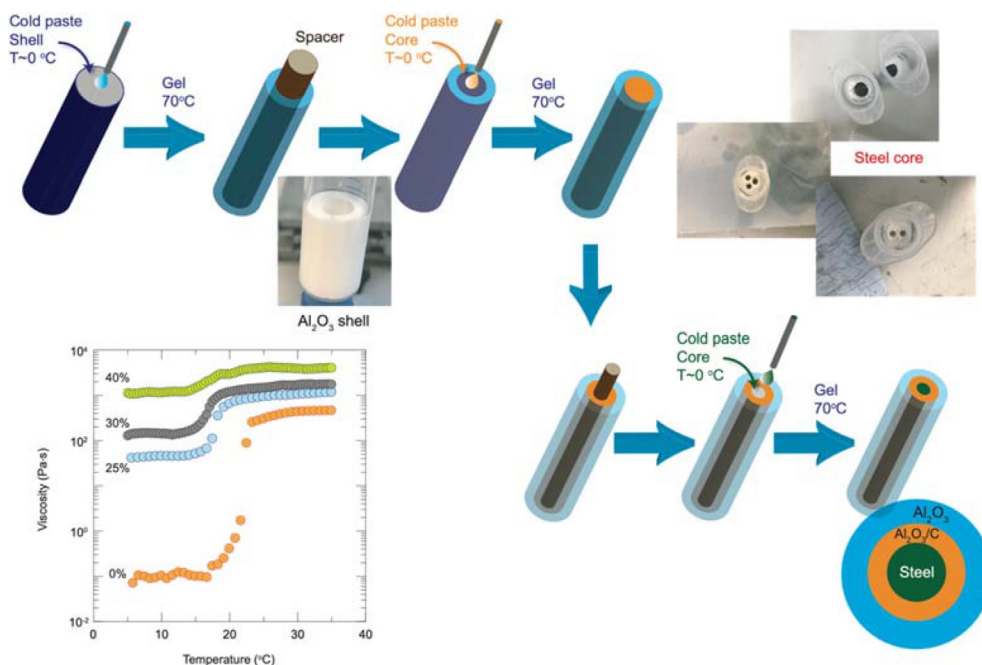
Fig. 1. Process of preparing printing cartridges with core–shell structure using thermally reversible hydrogels. The graph shows the variation of viscosity with temperature for gels with different Al₂O₃ contents (in vol%). The solid content does not have a measurable effect on the initiation of the liquid-gel transition that takes place at around 18 °C allowing printing at room temperature. By playing with the temperature and a set of spacers it is possible to create cartridges with a core shell structure including one to three cores. In order to engineer the interphase between the core and the shell we use a series of spacers of decreasing diameter.

gas. Afterwards, the syringe was placed again in the hot bath to gel the core. In order to create an interlayer between the steel core and the ceramic shell the process was conducted in three steps: i) an alumina suspension was gelled in the syringe and a large cylindrical spacer is placed in it; ii) an Al_2O_3/C (90/10 in vol%) ink was introduced in the cylindrical hole and gelled. A smaller cylindrical spacer was placed in the middle and removed; iii) the hole was filled with the cold steel paste and the temperature was raised to gel it.

The rheology of the pastes was characterized using a Discovery HR-1 hybrid rheometer (TA instrument, UK) with a 40 mm parallel plate geometry. The testing gap was 1 mm and a solvent trap was used to prevent drying. Temperature ramp tests were conducted from 0℃ to 40℃ (-5℃ to 20℃ for the 40 wt% Pluronic solution) at a shear rate of $1\ s^{-1}$. The flow ramp tests were set at 20 ℃ at shear rates ranging from $0.01\ s^{-1}$ to $100\ s^{-1}$. Oscillation amplitude sweep tests were carried out at 1 Hz with oscillation stresses ranging from 1 Pa to 1000 Pa.

The green bodies (woodpile structures and bars) were printed on flat, smooth substrates (polished poly tetra fluoroethylene or steel) using a direct ink writing system (3D inks LLC, USA). A thin layer of grease was applied to the substrates to facilitate removal of the printed part. The core–shell printing cartridges were loaded in the system and extruded through conical plastic or straight steel nozzles with diameters ranging from 0.1 to 1.56 mm. The printing temperature was maintained at 23℃ and the humidity was kept between 65 % and 85 % with a humidifier.

The printed green bodies were dried in a controlled environment at room temperature (20 to 25℃) and 60 to 70 % humidity overnight to avoid bending and cracking. After that, they were removed from the substrate carefully. When printing dense parts, filament overlapping was adjusted to avoid gas trapping following a process described elsewhere [24]. The green bodies of the bars were cold isostatic pressed after drying (CIP, Stansted Fluid Power ltd, UK) at 300 MPa to enhance densification and close large defects. The green density of the pressed samples is estimated to

be ∼ 40–50 th%. The samples were sintered in vacuum (10^{-6} torr). First, the dried green bodies were fired in vacuum at 600℃ for 2 h to burn out the Pluronic. Next, they were sintered at 1400 ℃ for 2 h, with heating and cooling rate of 5 ℃/min. Under these conditions, volatilization of iron and chromium from the alloy encapsulated by the dense ceramic is expected to be minimal [25].

Compression tests were performed in woodpile structures (8 mm × 6 mm × 1.5 mm) printed with a 410 μm nozzle using a universal testing machine (Zwick/Roell Z2.5). The top and bottom surface of the grids were polished to ensure they were parallel. The same nozzle was used to print bars for mechanical tests. Four-point bending strength was measured using as-printed bars (25 × 2.5 × 2.5 mm) or after polishing their tensile surfaces down to 1 μm diamond. The bottom span was 21 mm and the top span was 10 mm. The displacement rate was 0.2 mm/min. Three-point bending tests on Single-Edge Notched Bend (SENB) samples were performed ex-situ (Instron 8562, US) to measure toughness. The notches were made in two steps. First, a 0.84 mm thickness diamond wafer blade was used to cut a large notch in a bar with a depth of about 1/3 of the sample thickness. Then, a razor blade and 1 μm diamond suspension was used to sharpen the notch by reciprocating cutting. A force between 2 N and 10 N was applied during notching to ensure that the razor blade was in contact with the sample with breaking the samples (the force was increased gradually). The span was 15 mm, the displacement rate was 5 μm/min and a Linear Variable Differential Transformer (LVDT) was used to monitor displacements. The value of K_{IC} was calculated using the load at which the slope of the force–displacement curve starts to decrease indicating the formation of a crack from the notch (ASTM 1820–11). In-situ three-point bending tests were also performed on notched bars to visualize crack propagation and in single extruded filaments with a diameter ∼300 μm. The span was 21 mm and the displacement rate 1 mm/min. All in-situ tests were performed in the scanning electron microscope (Zeiss Sigma 300, Germany) using a microtest stage (MT300 Tensile Tester,

DEBEN, UK). Three to five samples were measured in each mechanical test.

The density of the samples was measured using the Archimedes method and the porosity calculated employing the theoretical density calculated using the predicted volume fraction of steel in the sample. The composition and microstructure of the samples and as received powders was analyzed using X-ray diffraction (2θ ranged between 6° to 90°, the scanning speed was 4°/min and the step size was 0.043°) and optical and scanning electron microscopy (JSM 6010LA, JEOL, Japan) with associated energy dispersive spectroscopy. Image analysis (Image J, NIH, USA) of scanning electron micrographs taken from polished cross section was used to calculate the steel volume fraction in sintered samples.

Finite element modelling of the residual thermal stresses in the steel-alumina core–shell structure generated during cooling from 1400 °C to room temperature was carried out using the ABAQUS platform. The dimensions measured from SEM images were used for the modelling of the fibres and matrix. The edges of single filament were set free and the simplified bars were simulated using symmetric boundary conditions to reduce the simulation size and allow for smaller elements. Due to the simple geometry, a number of 163404 C3D8R hexagonal elements were used. The plastic deformation of the steel was considered during cooling and the Poisson's ratio, modulus of elasticity and modulus of plasticity were all varied with temperature (Table 1) [26,27].

3. Results

3.1. Paste rheology and printing

All the alumina and steel pastes exhibit a transition between a liquid-like behavior with relatively low viscosity at low temperature and a printable gel at high temperature. The transition temperature depends on the Pluronic and solid content and typically ranges between 15 and 20 °C what enables room temperature printing (Fig. 1). At room temperature, all pastes behave as a gel at low stresses (G'>G", where G' and G" are the storage and loss moduli respectively), exhibit a shear thinning behavior and show a 'gel to liquid' transition, when G" becomes larger than G', at a given stress (the flow point). Increasing the solid content increases both the storage modulus in the linear regime (region for which G' does not change with applied stress) and the flow point (Fig. 2, Table 2). This behavior enables the preparation of the core–shell cartridges. At low temperature the inks flow well and fill the space without trapping gas. When introducing the cold core ink, the shell

is a gel, its yield stress and storage modulus are high enough to avoid deformation and retain the concentric arrangement.

During printing it was observed that the use of a paste with 35 vol% content of alumina in the shell combined with a paste containing 30 vol% of steel in the core enabled co-extrusion of filaments with the desired core–shell structure in which the ceramic shell encapsulates a continuous metallic filament. A paste containing 35 vol% of a 1/9 mixture in volume of C and Al_2O_3 can also be co-extruded to create a continuous interlayer. The goal in this latter case is to generate a porous interphase to promote crack deflection by burning the C during sintering.

The core–shell cartridges were used to extrude single filaments and print lattices with a woodpile structure. After sintering at 1400 °C in vacuum, the filaments retain their shape. In the filaments containing multiple cores, they do not fuse and remain as isolated fibers (from 1 to 3) in a matrix. The cores do not exhibit an ideal cylindrical cross section and their equivalent diameter ranges between ~ 130 μm for the one core system and ~ 80 μm in average for the two and three core systems and the one with the C interface fabricated with smaller diameter spacers. The steel content is similar for sintered bars and filaments and is given in Table 3. When there is no intermediate layer, there is a sharp interface between steel and Al_2O_3 with no evidence of mixing during extrusion. This interface is also rough at the microscopic level, with the roughness approximately corresponding to the size of the steel particles. The main components of the steel (Fe and Cr) do not to react with alumina during sintering in vacuum (Fig. 3). When extruding with a C-Al_2O_3 interlayer, the carbon burns out during firing and results in the formation of a microporous interphase between the steel fiber and the alumina matrix. The thickness of the interlayer varies between ~ 10 to 50 μm. There is no evidence of chemical reaction between the steel and the carbon (Figs. 3 and 4).

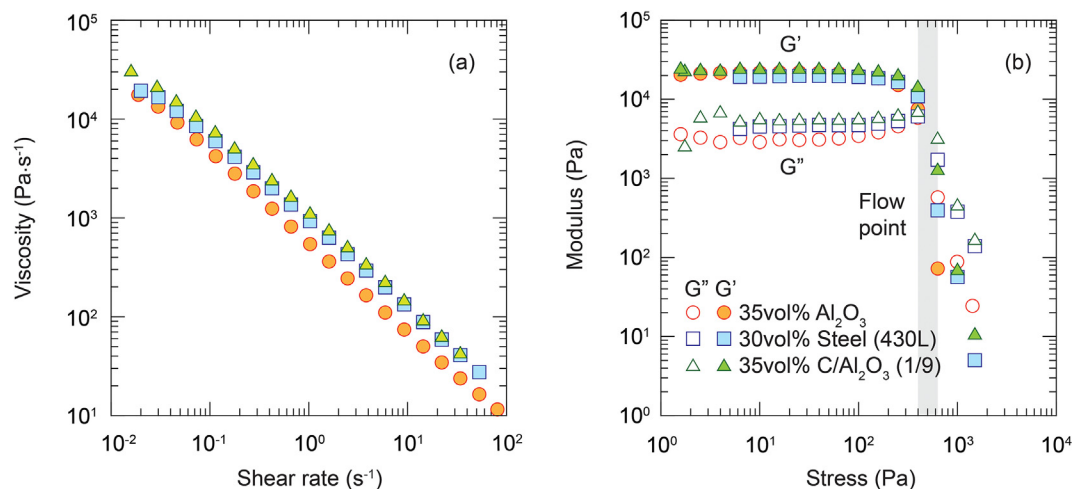### 3.2. Mechanical properties of single filaments and woodpile structures

The single-phase Al_2O_3 filaments are brittle as expected (Fig. 5). The behavior of the core–shell filaments is more complex; although the shell breaks in a brittle manner, the ductile core deforms plastically and holds the filament together while the load reaches a plateau (Fig. 5). The bending strengths of Al_2O_3 filaments with a diameter of ~ 300 μm are of the order of 400 ± 150 MPa. These strengths are comparable to those of Al_2O_3 ceramics fabricated through more conventional technologies. The inclusion of one or two steel cores in the filament increases significantly the

Table 1
Density, thermal expansion, plasticity, elastic modulus and Poisson's ratio of steel and Al_2O_3 used for finite element modelling [26,27].

Material	Density (kg/m^3)	Thermal Expansion (10^{-6}/°C)	Plastic			Elastic modulus (GPa)	Poisson's ratio
			Temperature (K)	Yield stress (MPa)	Plastic strain (%)		
Core: steel	7700	12	300	400	0	200	0.29
				500	0.1		
			700	280	0		
				320	0.1		
			900	50	0		
				55	0.1		
			1400	10	0	100	0.36
				11	0.1		
Shell: Al_2O_3	3970	8	300			370	0.24
			700			360	0.24
			1100			350	0.26
			1300			340	0.31
Interphase: Al_2O_3		8	300			300	0.22
			700			290	0.22
(10 % porosity)	3570		1100			280	0.25
			1300			280	0.29

Fig. 2. Rheology of the pastes used in the printing process. (a) Variation of the viscosity with shear rate. The viscosity of the pastes and their shear thinning coefficients match (n ∼ 0.1). (b) The viscoelastic response of the pastes also matches with similar storage modulus and flow points.

Table 2
Summary of the rheology of pastes formulated in this work. The shaded compositions are those that could be co-extruded. In the table τ_{fp} is the flow point (stress for which G'=G" in oscillatory tests); K is the viscosity parameter and n is the shear thinning coefficient as defined in equation (1).

| Inorganic content (vol%)	n	K (Pa·s^{-n})	G' (kPa)	τ_{fp} (Pa)
30 % (Al$_2$O$_3$)	0.22	1145	1.956 ± 126	381 ± 73
35 % (Al$_2$O$_3$)	0.12	7867	19.542 ± 224	581 ± 117
40 % (Al$_2$O$_3$)	0.14	13,986	23.182 ± 51	963 ± 189
45 % (Al$_2$O$_3$)	0.44	7036	30.161 ± 118	1117 ± 250
35 % (C/Al$_2$O$_3$)	0.09	12,722	24.825 ± 258	583 ± 116
30 % (Steel)	0.09	6256	21.545 ± 595	577 ± 117
35 % (Steel)	0.24	4317	37.649 ± 226	641 ± 185

Table 3
Density of sintered samples printed with 410 μm nozzles and volume fraction of steel, V_f^s, calculated from the starting composition or measured experimentally using image analysis.

Sample	$\rho_{experimental}$(g/cm^3)	$\rho_{theoretical}$(g/cm^3)	$(V_f^s)_{experimental}$	$(V_f^s)_{theoretical}$	Porosity
Al$_2$O$_3$	3.67 ± 0.05	3.97	–	–	7.6 %
1-core	4.48 ± 0.07	4.85	0.20 ± 0.02	0.23	7.6 %
2-core	4.27 ± 0.06	4.52	0.14 ± 0.01	0.15	5.5 %
3-core	4.63 ± 0.07	4.81	0.22 ± 0.02	0.22	3.7 %
C-interphase	3.76 ± 0.05	4.24	0.07 ± 0.01	0.07	11.3 %
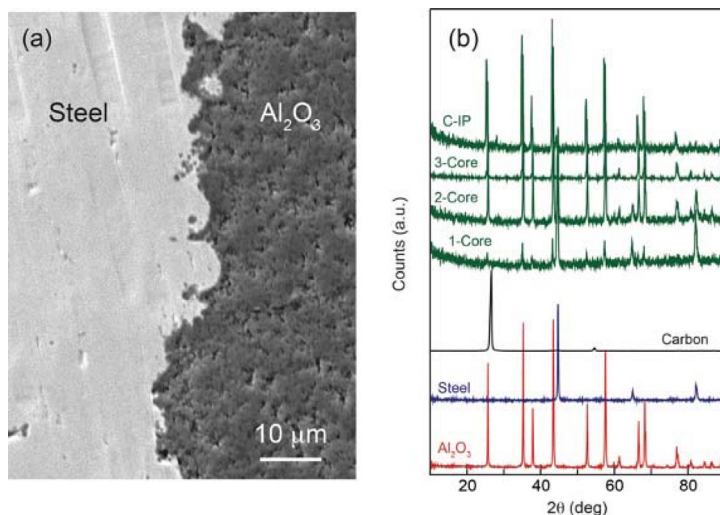
Fig. 3. (a) Scanning electron micrograph showing the interface between steel and alumina after sintering. (b) X-ray diffraction patterns of the starting powders and sintered samples. There are no additional phases after sintering and the C peaks are not visible in the samples prepared with the carbon interphase.
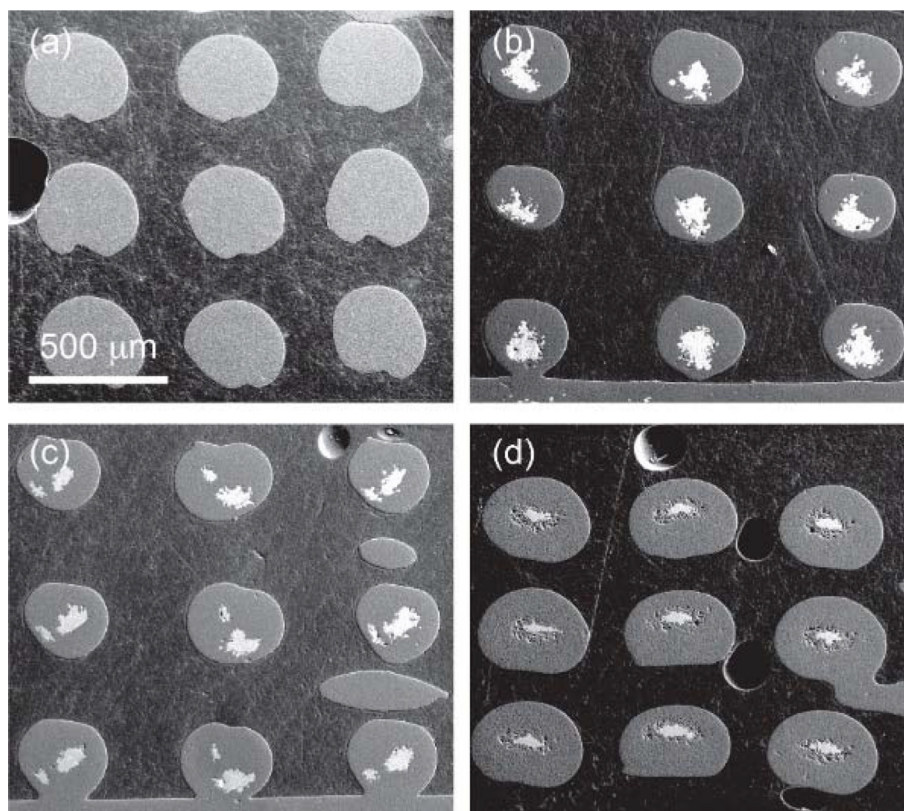
Fig. 4. Polished cross sections of a sintered woodpile structure fabricated using: (a) alumina filaments; (b) 1-core, (c) 2-core and (d) 1-core with a porous interlayer (generated using a C-Al$_2$O$_3$ ink,10/90 in vol% filaments. The steel is visible as the brighter phase in the filaments.
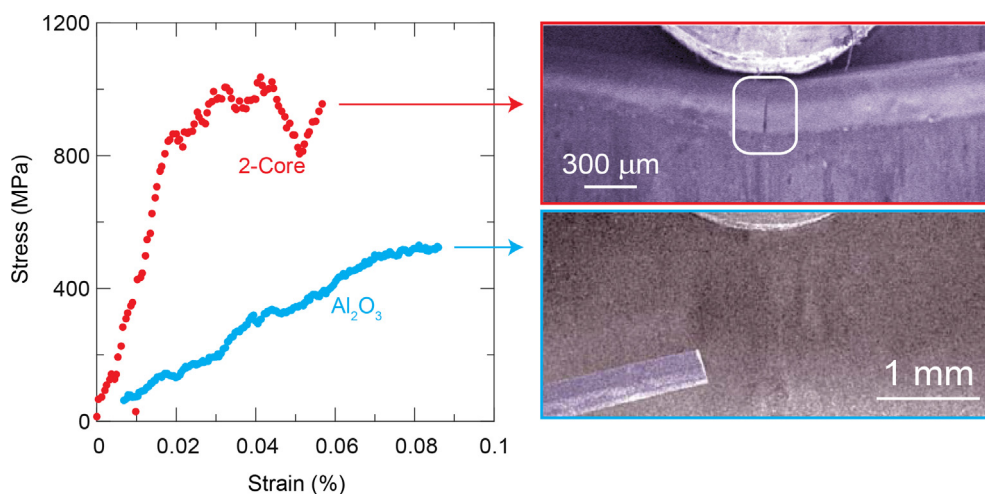

Fig. 5. Bending of single filaments. Alumina filaments are brittle. The addition of the steel cores increases the bending strengths and prevent brittle filament failure.

calculated strength that can approach values of 1 GPa (averages of 850 ± 350 and 700 ± 200 MPa for the 1 and 2-core systems respectively). However, filaments with three cores or with one core and a porous interphase are weaker (300 ± 100 MPa).

The response of the woodpile structures under compression reflects the effect of the metallic cores. The pure Al$_2$O$_3$ ones exhibit the type of failure previously observed on ceramic grids and foams with brittle struts or walls failing sequentially (individual dips in the load–displacement curves) to reach a plateau in the stress–strain curves until the whole structure fails and is unable to hold any load (Fig. 6) [28,29]. However, in lattices printed using core–

shell filaments the struts do not fail in a brittle manner but rather show extensive buckling. The lattices behave elastically and retain the stiffness of the ceramic up to the peak stress but do not exhibit the same brittle behavior (Fig. 6). The maximum load is reached when the ceramic shell fails and the steel core buckles. The maximum stresses are significantly higher than those measured on the ceramic grids and, with the exception of the core–shell lattices with the porous interlayers, they are able to sustain substantial loads of tens of MPa even after relatively large deformations. The energy absorption capabilities are also much larger.
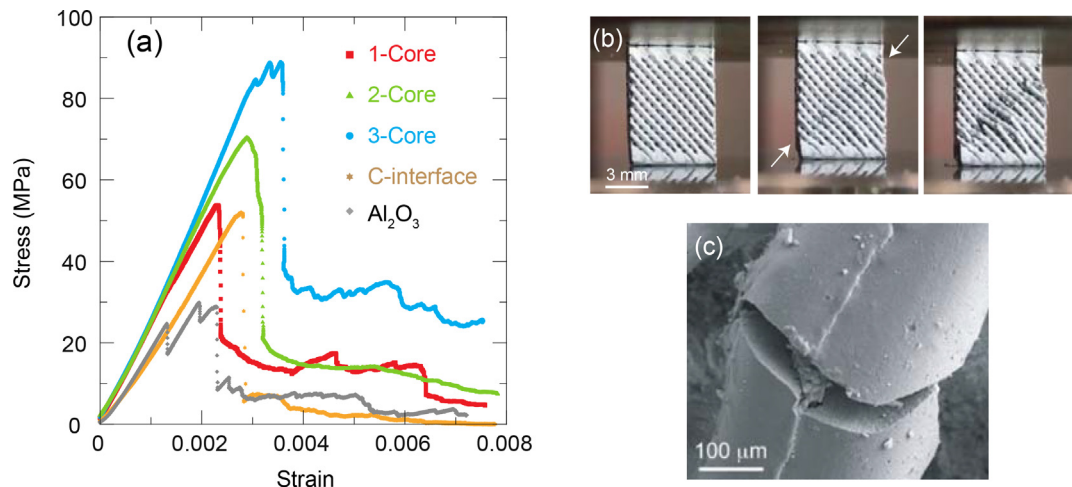
Fig. 6. (a) Stress displacement curves from compression tests performed on the woodpile structures. The ceramic grids break in the gradual manner observed in other ceramic woodpile structures with drops corresponding to individual strut failures. In the structures with steel cores the struts fail by buckling and they retain strength even after relatively large displacements (b) Stills taken during the compression of a 3-core wood pile structure clearly show buckling of the struts along a kink band (white arrows) (c) SEM micrograph of a fractured filament (3-core) in a woodpile structure. The ceramic shell has broken but the steel fibres are still able to maintain it together.

3.3. Mechanical properties of dense structures

The system was used to print dense parts for bending tests. After CIP and sintering the samples are relatively dense (porosities $\sim$ 11 % for the sample with the porous interface and between 3 and 8 % for the others) and free of large defects. Most of the microporosity is concentrated in the matrix or in the porous interlayer. This could be expected as the sintering temperatures are slightly lower than those conventionally used to sinter alumina. The metal fibers are continuous but their cross section has been distorted (Fig. 7). The final metal content of the materials estimated using image analysis ranges between 7 and 25 vol% depending on the number of cores. The experimental values correspond well to those calculated from the relative radii of the syringe and the spacers used to generate the shell (Table 3).

The printed alumina bars are brittle and their bending strengths, of the order of 200 MPa, are similar to those reported for robocasted ceramics of similar composition (Fig. 7). [30] The metallic fibers increase significantly the average strength (up to $\sim$ 350 MPa for 1 and 2-core samples) and change the behavior

towards a more gradual, "graceful" failure in notched samples (Fig. 8). The exception are the samples with porous interphases that are brittle, like the monolithic ceramics, and with similar strengths. The fracture surfaces show extensive plastic deformation of the fibers (Fig. 7). Overall, the bars, even those whose tensile face has been polished before testing, are weaker than the corresponding single filaments and the relative increase of strength achieved by introducing the metallic fibers is lower.

The introduction of the fibers almost doubles the K_{IC} measured using notched samples (Fig. 8). This value is measured at the load at which the compliance of the sample starts to increase during bending and represents the resistance to the growth of short cracks from the notch. The addition of the steel fibers has a substantial effect on the work of fracture that increases proportionally to the steel content of the material up to 1400 J/m^2 for the samples with the largest steel content (Fig. 8).
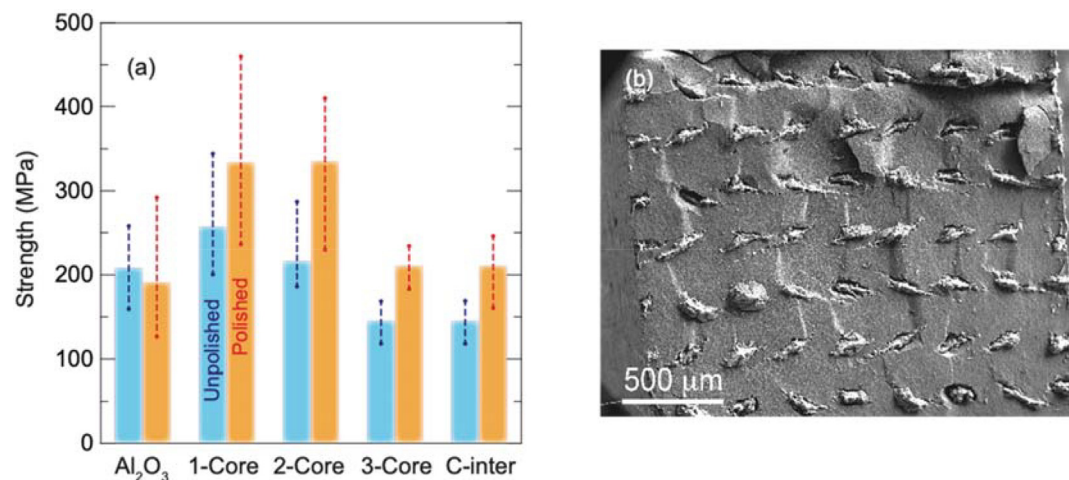
Fig. 7. (a) Bending strengths of polished and unpolished bars. The inclusion of fibers increases the strength but the porous fiber–matrix interlayer decreases it. Polishing the tensile surface has an effect on the strength of the fiber-reinforced materials suggesting the importance of surface flaws. (b) Fracture surface of a 1-core bar after a bending test. Plastic deformation of the steel fibers is visible.
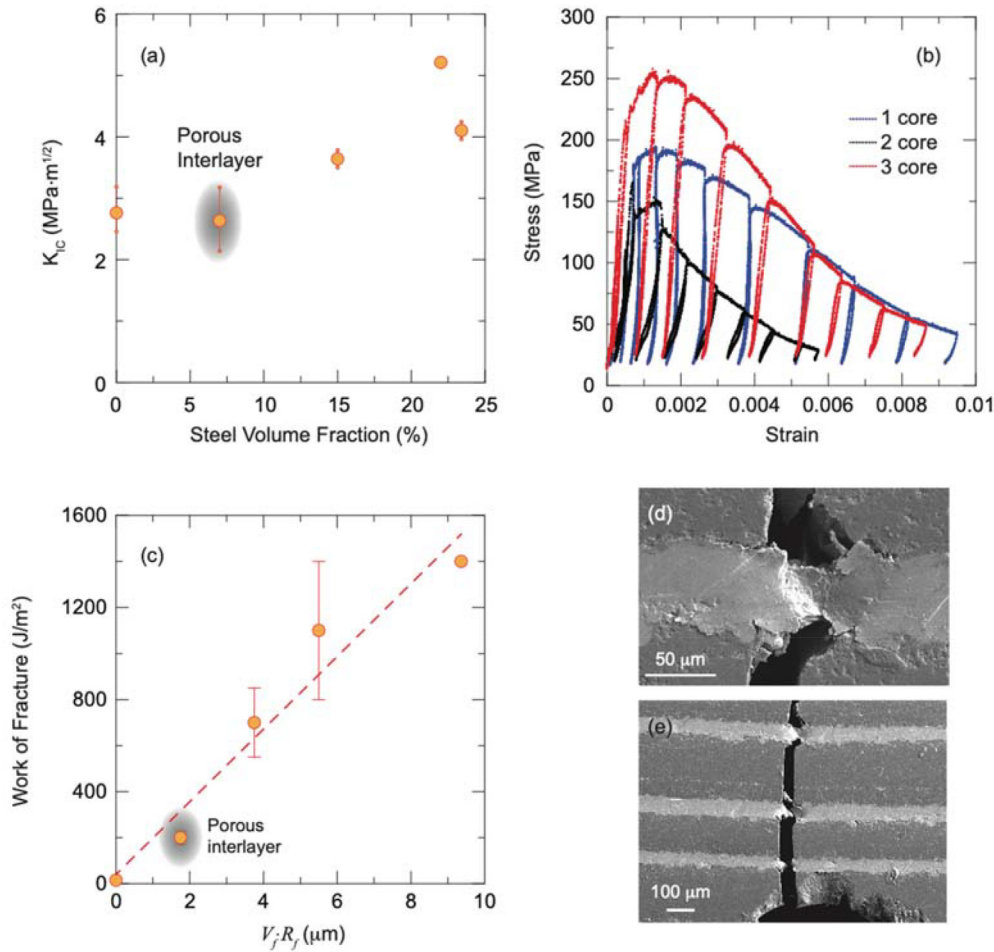
Fig. 8. (a) K_{IC} of the different composites. Toughness increases with steel content. (d) The stress–strain cyclic curves for notched samples. The steel fibers induce a "graceful" gradual failure. The loading and unloading curves from different cycles remain parallel underlining the role of plasticity. (e) Works of fracture. The linear fitting corresponds to $s_f = 0.125$ using eq. (4). The figure shows crack bridging and metallic fiber plastic deformation. The deformation concentrates around the fracture surface what is consistent with the calculated s_f.

4. Discussion

A printable paste for robotic assisted deposition should exhibit a shear thinning behavior and a yield stress. [31] In this way, it can flow under pressure through the nozzle during printing and hold the weight of the part without deformation. The rheology of these shear thinning pastes is often described using the standard Herschel-Bulkley model [32]:

$$\tau = \tau_y + K\dot{\gamma}^n \tag{1}$$

where τ_y is the yield stress, K is the viscosity parameter, n is the shear thinning coefficient (that is < 1 in a shear thinning paste) and $\dot{\gamma}$ is the shear rate. In order to calculate K and n more accurately, fitting to a simple power law $\tau = K\dot{\gamma}^n$ at intermediate shear rates is often used (Table 2) [4]. To enable co-extrusion through a single nozzle, all the pastes (core, shell and interlayer) have to flow in a continuous manner through the nozzle at the constant piston displacement rate and the core should retain its shape to create a continuous cylindrical fiber in the matrix. Our results suggest that it is necessary to match the rheological parameters in particular the yield stress, and shear thinning coefficient to ensure that there are no discontinuities in the velocity profile across the radius of the printing nozzle. For a cylindrical nozzle, the velocity at a distance r from the center is given by [33]:

$$V(r) = \frac{nR}{\tau_\varpi(n+1)} \left(\frac{1}{K}\right)^{\frac{1}{n}} \left[(\tau_\varpi - \tau_y)^{\frac{n+1}{n}} - \left(\frac{\tau_\varpi r}{R} - \tau_y\right)^{\frac{n+1}{n}} \right] \tag{2}$$

where R is the total radius of the nozzle, and τ_w is the drag at the wall. By matching the parameters in equation (1) we can assume that the system behaves as if we were essentially extruding the same paste through the nozzle. This is achieved by using suspensions based on the same formulation and manipulating the solid and Pluronic content of the paste (Fig. 2).

The solid contents of the pastes, above 30 vol%, are large enough to ensure densification during sintering [30]. In addition, the particles are immersed in a Pluronic gel, whose properties enables the preparation of stable suspensions using relatively dense particles (like steel) without sedimentation and the mixing of particles with different densities forming a stable paste [34]. Finally, Pluronic has hydrophilic and hydrophobic groups what allows the preparation of dense, homogeneous pastes containing hydrophobic and hydrophilic particles (Al_2O_3 and C). The storage moduli in the linear region of the inks used in co-extrusion are the order of 20–25 kPa and the flow points are of the order of 580 Pa. The ratio between storage modulus and flow point is often used as an indication of printability as it gives the balance between the pressure needed for extrusion that is dictated by the flow point/yield stress and that should be relatively low, and the ability to bridge spans in cellular structures without sagging. In our case this ratio ranges

between 35 and 50, well in the range of what is considered acceptable [35,36].

As expected, the alumina filaments are brittle. However, in the filaments with an internal metallic fiber, first the ceramic shell breaks and then the steel can hold the load while bending. This could be expected as the fracture strain of 430L steel is around 3 orders of magnitude larger than the failure strain of alumina [37]. The relatively high strength of the alumina filaments can be attributed to their small radius that limits the defect size. The toughness of the fine-grained alumina is $\sim$ 2–3 MPa·m$^{1/2}$ (Fig. 8), suggesting a critical defect size of the order of 10 μm that is reasonable in comparison with the filament diameter. The relatively large variability in strengths point out to a wide defect distribution that can result from the preparation (trapped bubbles) and handling of the single filaments and the fact that their surfaces are not polished. The addition of one or two steel cores increases the strength. In these filaments, the ceramic volume is smaller and the ceramic shell is expected to be under compression in the axial direction due to the thermal stresses arising from the difference in thermal expansion between alumina and steel. As the number of steel fibers inside a single filament increases to 3 the strength decreases. The increase in the number of cores or the introduction of a porous interphase can lead to the generation of larger defects that are detrimental for strength. Distortion is larger in filaments with 3 cores where in some case the steel fibers can merge (Fig. 9).

The response of the woodpile structures is very similar to the one reported for polymeric lattices combining flexible and brittle epoxies in similar core–shell arrangements [15]. The comparison of the behavior of single filaments and the lattices suggests that the samples with porous interlayers contain more defects and thinner cores that are detrimental both to their peak strength and their ability to sustain load after the steel fiber has buckled.

In the case of the dense bars there is a clear distortion of cross section of the metallic fibers that have been flattened (Fig. 7). This distortion arises during printing as in order to ensure densification each printed line is slightly pressed against the previous one (each height step during printing is slightly below the filament diameter). Cold isostatic pressing prior to sintering is used to eliminate pores trapped between printing lines (Fig. 10).

The alumina bars are significantly weaker than the single filaments. The metallic fibers increase the strength but this increase is not at the same level than the one measured in the single filaments. In the FE calculations with ideal cylindrical steel fibers of similar average diameter, the compressive axial stresses in the matrix can be as high as $\sim$ 240 MPa for the 1-core system
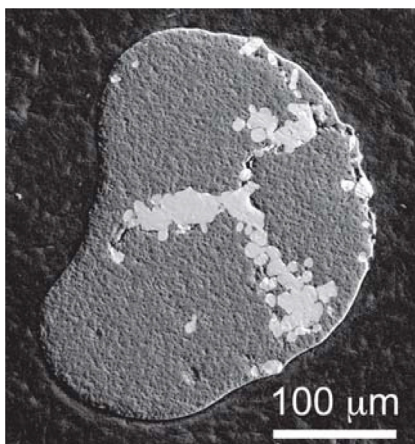

Fig. 9. Scanning electron micrograph of the polished cross section of a sintered filament with 3 cores. In this system the metallic cores are highly distorted during extrusion.

(Fig. 11). The addition of cores decreases these stresses to $\sim$ 100 MPa for the 2-core and $\sim$ 60 MPa for the 3-core system. The porous C interface also decreases the compressive axial stresses in the 1-core system to around $\sim$ 60 MPa. The magnitude of the compressive stresses could explain partially the decrease in bending strengths after introducing one and two cores. It can also be observed that the strengths of filaments and polished or non-polished bars also decrease with an increase in the number of cores and the corresponding decrease of residual compressive stresses in the matrix. However, it has to be recognized that the model is a simplified version of the microstructures with circular steel fibers. In reality the fibers in the dense bars can be highly deformed (Figs. 7 and 9) and the FEM results should be taken as an indication of the expected trends.

Using the relationship between toughness, strength and defect size, the critical defect size in the alumina bars would be around four times that of the filaments. Larger defects are expected in the bars, for example defects generated by gas trapping between the printed filaments that could remain to some extent even after cold isostatic pressing (Fig. 10). The bars are rougher and can also exhibit larger surface defects: the strength of unpolished samples is similar for all materials, after polishing and removing surface defects, the strength of samples containing fibers increases 30 to 40 % (Fig. 7). The larger defects could explain why the increase in strength is proportionally smaller in the bars.

The increase in K_{IC} with the introduction of fibers is mostly due to the introduction of compressive thermal stresses in the matrix (Figs. 8 and 10). However, in these materials most of the toughening will come from extrinsic mechanisms acting at larger crack lengths. Because the fine-grained alumina samples are brittle their work of fracture is better estimated using the critical energy release strain rate G_{IC}.

$$G_{IC} = \frac{K_{IC}^2}{E} \tag{3}$$

where E is the Young modulus of alumina (taken to be 350 GPa). In this case G_{IC} is of the order of 10–25 J/m^2. The introduction of the fibers increases the work of fracture (W_f) up to two orders of magnitude. We can use the model proposed by Pemberton et al. [38] to quantify the contribution of the metallic fibers to the work of fracture of the composites. In the absence of extensive pull-out at the fiber matrix interface:

$$W_f = \frac{2V_f s_f R W_d}{\varepsilon_*} \tag{4}$$

where V_f is the volume of fibers and R their average radius, W_d is the work of deformation of the fibers and ε_* their strain to failure (taken to be 120 MJ/m^3 and 0.25 at room temperature respectively) [37] and s_f is a fiber deformation aspect ratio, i.e. the ratio of the mean de-bonded length over the fiber radius. The model can approximate well the measured values with s_f = 0.125. This is a de-bonding length below the fiber radius what is consistent with the strong fiber–matrix adhesion observed in "in-situ" testing. The results suggest that plastic deformation of the fibers is the main reason of the large increase in work of fracture (Fig. 8). This is in agreement with the SEM observations of crack propagation (Fig. 8) and stress/strain curves recorded in multi-cycle bending tests where the slopes of loading and unloading cycles remain constant, with an increase in accumulated plastic strain at each cycle (Fig. 8). Because the main contribution to the work of fracture is from the plasticity of the fiber, unlike in ceramic-fiber composites, fiber pull-out does not play a significant role and the introduction of the porous interlayer does not have a beneficial effect. It reduces the final work of fracture as a consequence of the smaller fiber diameter (smaller steel content, Table 3) and decreased interfacial bonding.
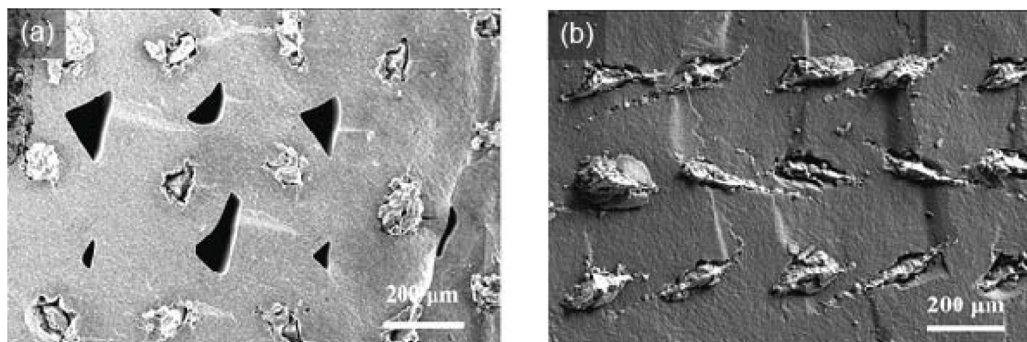
Fig. 10. Scanning electron micrographs of the fracture surfaces of printed bars (1-core filaments) (a) without CIP after printing and (b) with CIP. Isostatic pressing helps to close pores trapped between the printed lines and is used for all the bars tested in this work.
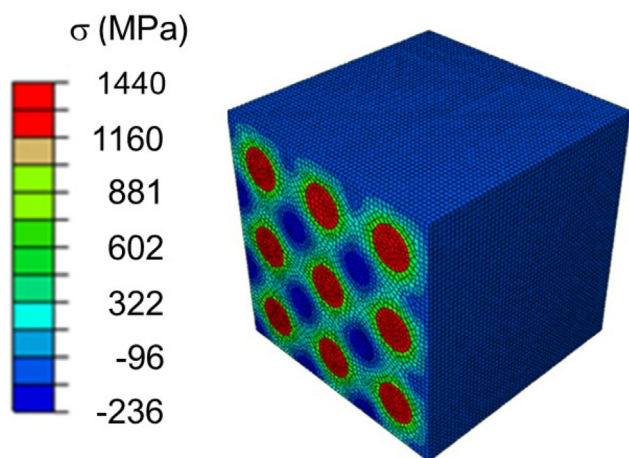
Fig. 11. Finite element calculations of thermal stresses parallel to the steel fibers after cooling from 1400 °C in a composite fabricated with a 1-core filament. A compressive stress develops in the alumina matrix.

5. Conclusion

We have developed a method to print cellular structures and dense ceramic matrix composites reinforced with continuous fibers following a computer design. Here, the approach is demonstrated with the printing of alumina reinforced with ductile steel fibers. The approach is based on the continuous extrusion of filaments with a core–shell structure using pastes based on thermally reversible hydrogels. To achieve co-extrusion of continuous fibers it is necessary to match the shear thinning coefficients and flow point of the pastes forming the core and the shell. The flow points (550–600 Pa) and storage modulus (20–25 kPa) of the pastes are also in the range needed to enable printing of parts able to retain their shape. The process can also be adapted to build interlayers between core and shell in a way that will be very difficult to achieve using other set-ups. We have used the process to build cellular structures and dense composites whose microstructure is designed to retain the stiffness of the ceramics while exhibiting much increased energy adsorption capabilities and works of fracture that can be up to two orders of magnitude that of the matrix. The approach can be extended to other fiber–matrix combinations and could open new possibilities in the design of composite parts with complex shapes for a wide range of applications from aerospace to healthcare.

References

[1] N.P. Bansal, J. Lamon, American Ceramic Society., Ceramic matrix composites : materials, Modeling and Technology, Wiley, Hoboken, New Jersey, 2015.
[2] J. Chevalier, A. Liens, H. Reveron, F. Zhang, P. Reynaud, T. Douillard, L. Preiss, V. Sergo, V. Lughi, M. Swain, N. Courtois, Forty years after the promise of << ceramic steel?>>: Zirconia-based composites with a metal-like mechanical behavior, J. Am. Ceram. Soc. 103 (3) (2020) 1482–1513.
[3] C. Piconi, S. Sprio, Oxide bioceramic composites in orthopedics and dentistry, J Compos Sci 5 (8) (2021).
[4] V.G. Rocha, E. Saiz, I.S. Tirichenko, E. Garcia-Tunon, Direct ink writing advances in multi-material structures for a sustainable future, J. Mater. Chem. A 8 (31) (2020) 15646–15657.
[5] J. Sun, D. Ye, J. Zou, X.D. Chen, Y. Wang, J. Yuan, H. Liang, Q. H., J. Binner, J. Bai, A review on additive manufacturing of ceramic matrix composites, J. Mater. Sci. Technol. 138 (2023) 1-16.
[6] B.G. Compton, J.A. Lewis, 3D-printing of lightweight cellular composites, Adv. Mater. 26 (34) (2014) 5930-+.
[7] E. Feilden, C. Ferraro, Q.H. Zhang, E. Garcia-Tunon, E. D'Elia, F. Giuliani, L. Vandeperre, E. Saiz, 3D printing bioinspired ceramic composites, Sci. Rep. 7 (2017).
[8] G. Franchin, L. Wahl, P. Colombo, Direct ink writing of ceramic matrix composite structures, J. Am. Ceram. Soc. 100 (10) (2017) 4397–4401.
[9] Y.L. Xia, Z.L. Lu, A.J.W. Cao, K. Miao, J. Li, D.C. Li, Microstructure and mechanical property of Cf/SiC core/shell composite fabricated by direct ink writing, Scr. Mater. 165 (2019) 84–88.
[10] N.P. Padture, Advanced structural ceramics in aerospace propulsion, Nat. Mater. 15 (8) (2016) 804–809.
[11] K.R. Hart, R.M. Dunn, E.D. Wetzel, Tough, additively manufactured structures fabricated with dual-thermoplastic filaments, Adv. Eng. Mater. 22 (4) (2020).

[12] C. Kaya, E.G. Butler, M.H. Lewis, Co-extrusion of Al2O3/ZrO2 bi-phase high temperature ceramics with fine scale aligned microstructures, J. Eur. Ceram. Soc. 23 (6) (2003) 935–942.

[13] C. Van Hoy, A. Barda, M. Griffith, J.W. Halloran, Microfabrication of ceramics by co-extrusion, J. Am. Ceram. Soc. 81 (1) (1998) 152–158.

[14] R.P. Wilkerson, B. Gludovatz, J. Watts, A.P. Tomsia, G.E. Hilmas, R.O. Ritchie, A novel approach to developing biomimetic ("Nacre-Like") metal-compliant-phase (nickel-alumina) ceramics through coextrusion, Adv. Mater. 28 (45) (2016) 10061–10067.

[15] J. Mueller, J.R. Raney, K. Shea, J.A. Lewis, Architected lattices with high stiffness and toughness via multicore-shell 3D printing, Adv. Mater. 30 (12) (2018).

[16] R.C. Pack, S.K. Romberg, A.A. Badran, N.S. Hmeidat, T. Yount, B.G. Compton, Carbon fiber and syntactic foam hybrid materials via core-shell material extrusion additive manufacturing, Adv Mater Technol-Us 5 (12) (2020).

[17] D.J. Lorang, D. Tanaka, C.M. Spadaccini, K.A. Rose, N.J. Cherepy, J.A. Lewis, Photocurable liquid core-fugitive shell printing of optical waveguides, Adv. Mater. 23 (43) (2011) 5055–5058.

[18] A. Le Duigou, A. Barbe, E. Guillou, M. Castro, 3D printing of continuous flax fibre reinforced biocomposites for structural applications, Mater Design 180 (2019).

[19] F. Peng, D.V. Vogt, M. Cakmak, Synergistic material extrusion 3D-printing using core–shell filaments containing polycarbonate-based material with different glass transition temperatures and viscosities, Int. Polym. Proc. 37 (2022) 406–414.

[20] J.X. Zhao, H.Y. Lu, Y. Zhang, S.X. Yu, O.I. Malyi, X.X. Zhao, L.T. Wang, H.B. Wang, J.H. Peng, X.F. Li, Y.Y. Zhang, S. Chen, H. Pan, G.C. Xing, C.H. Lu, Y.X. Tang, X.D. Chen, Direct coherent multi-ink printing of fabric supercapacitors, Sci. Adv. 7 (3) (2021).

[21] Y.T. Zhou, Y.Z. Yang, A.J. Jian, T.R. Zhou, G.M. Tao, L.Q. Ren, J.F. Zang, Z.H. Zhang, Co-extrusion 4D printing of shape memory polymers with continuous metallic fibers for selective deformation, Compos. Sci. Technol. 227 (2022).

[22] C.J. Zeng, L.W. Liu, W.F. Bian, J.S. Leng, Y.J. Liu, Temperature-dependent mechanical response of 4D printed composite lattice structures reinforced by continuous fiber, Compos. Struct. 280 (2022).

[23] Y.W. Moon, I.J. Choi, Y.H. Koh, H.E. Kim, Macroporous alumina scaffolds consisting of highly microporous hollow filaments using three-dimensional ceramic/camphene-based co-extrusion, J. Eur. Ceram. Soc. 35 (16) (2015) 4623–4627.

[24] E. Feilden, Additive manufacturing of ceramics and ceramic composites via robocasting, Department of Materials, Imperial College of London, 2017.

[25] O. Kubaschewski, G. Heymer, The Thermodynamics of the Chromium-Iron System, Acta Mater. 8 (1960) 416–423.

[26] P. Auerkari, Mechanical and physical properties of engineering alumina ceramics, VTT Technical Research Centre of Finland, Espoo, 1996.

[27] M. Fukuhara, A. Sanpei, Elastic-Moduli and Internal-Friction of Low-Carbon and Stainless-Steels as a Function of Temperature, ISIJ Int. 33 (4) (1993) 508–512.

[28] P. Miranda, A. Pajares, E. Saiz, A.P. Tomsia, F. Guiberteau, Fracture modes under uniaxial compression in hydroxyapatite scaffolds fabricated by robocasting, J. Biomed. Mater. Res. A 83a(3) (2007) 646–655.

[29] L.J. Gibson, M.F. Ashby, Cellular solids : structure & properties, 1st ed., Pergamon Press, Oxford Oxfordshire; New York, 1988.

[30] E. Feilden, E.G.T. Blanca, F. Giuliani, E. Saiz, L. Vandeperre, Robocasting of structural ceramic parts with hydrogel inks, J. Eur. Ceram. Soc. 36 (10) (2016) 2525–2533.

[31] J.A. Lewis, J.E. Smay, J. Stuecker, J. Cesarano, Direct ink writing of three-dimensional ceramic structures, J. Am. Ceram. Soc. 89 (12) (2006) 3599–3609.

[32] W.H. Herschel, R. Bulkley, Konsistenzmessungen von Gummi-Benzollosungen, Kolloid-Zeitschrift 39 (1926) 291–300.

[33] S.m.M. Peker, S.e.S. Helvacı, Solid-liquid two phase flow, 1st ed., Elsevier, Amsterdam; Boston, 2008.

[34] E. Feilden, D. Glymond, E. Saiz, L. Vandeperre, High temperature strength of an ultra high temperature ceramic produced by additive manufacturing, Ceram. Int. 45 (15) (2019) 18210–18214.

[35] S.S.L. Chan, M.L. Sesso, G.V. Franks, Direct ink writing of hierarchical porous alumina-stabilized emulsions: Rheology and printability, J. Am. Ceram. Soc. 103 (10) (2020) 5554–5566.

[36] J.E. Smay, J. Cesarano, J.A. Lewis, Colloidal inks for directed assembly of 3-D periodic structures, Langmuir 18 (14) (2002) 5429–5437.

[37] M. Cortie, Effect of Temperature on the Resistance to Tearing of Type 430 Stainless-Steel Sheet, ISIJ Int. 34 (5) (1994) 443–450.

[38] S.R. Pemberton, E.K. Oberg, J. Dean, D. Tsarouchas, A.E. Markaki, L. Marston, T. W. Clyne, The fracture energy of metal fibre reinforced ceramic composites (MFCs), Compos. Sci. Technol. 71 (3) (2011) 266–275.